Testable polarization predictions for models of CMB isotropy anomalies

Cora Dvorkin,[1,2] Hiranya V. Peiris,[1,3*] and Wayne Hu[1†]
[1] *Kavli Institute for Cosmological Physics, Department of Astronomy & Astrophysics, and Enrico Fermi Institute, University of Chicago, Chicago IL 60637, U.S.A.*
[2] *Department of Physics, University of Chicago, Chicago IL 60637, U.S.A.*
[3] *Institute of Astronomy, University of Cambridge, Cambridge CB3 0HA, U.K.*
(Dated: November 15, 2007)

Anomalies in the large-scale CMB temperature sky measured by WMAP have been suggested as possible evidence for a violation of statistical isotropy on large scales. In any physical model for broken isotropy, there are testable consequences for the CMB polarization field. We develop simulation tools for predicting the polarization field in models that break statistical isotropy locally through a modulation field. We study two different models: dipolar modulation, invoked to explain the asymmetry in power between northern and southern ecliptic hemispheres, and quadrupolar modulation, posited to explain the alignments between the quadrupole and octopole. For the dipolar case, we show that predictions for the correlation between the first 10 multipoles of the temperature and polarization fields can typically be tested at better than the 98% CL. For the quadrupolar case, we show that the polarization quadrupole and octopole should be moderately aligned. Such an alignment is a generic prediction of explanations which involve the temperature field at recombination and thus discriminate against explanations involving foregrounds or local secondary anisotropy. Predicted correlations between temperature and polarization multipoles out to $\ell = 5$ provide tests at the $\sim 99\%$ CL or stronger for quadrupolar models that make the temperature alignment more than a few percent likely. As predictions of anomaly models, polarization statistics move beyond the *a posteriori* inferences that currently dominate the field.

I. INTRODUCTION

Several anomalies observed in the CMB data suggest a possible breaking of statistical isotropy on the largest angular scales. Broken isotropy would represent a radical revision of the standard cosmological model as statistical isotropy underlies all cosmological inferences. As such, it is important to test such claims by all means possible.

Specifically, the measurements from the *Wilkinson Microwave Anisotropy Probe* (WMAP) [1, 2, 3, 4] indicate an asymmetric distribution in power between the northern and southern ecliptic hemispheres [5]. Also, the data exhibit alignments in the temperature field; in particular, the observed quadrupole and octopole of the CMB are planar and mutually aligned, and this plane is oriented roughly orthogonal to the CMB dipole direction [6, 7].

The statistical significance of these preferred directions has been investigated by several authors [7, 8, 9, 10, 11, 12, 13, 14, 15, 16], but the *a posteriori* choice of statistics makes their interpretation difficult. Since measurements of the temperature field have already reached the cosmic variance limit, further information from it will not be forthcoming, barring improvements in foreground and systematics modeling. On the other hand, large-scale CMB polarization measurements are still in their infancy and provide fertile grounds for future tests of isotropy. In particular, any physical model that purports to explain the temperature anomalies provides testable predictions for the statistics of the polarization field.

In this *Paper*, we develop the radiative transfer tools required to investigate polarization statistics. Large-angle polarization arises from rescattering of CMB radiation from recombination during reionization. Given a model that predicts the statistical properties of the temperature field at recombination, Monte-Carlo realizations of the polarization field can be generated and analyzed for signatures of broken isotropy.

We apply these techniques to models that break statistical isotropy with a multiplicative modulation field [17]. These models posit that the observed temperature field is the product of a modulating field with superhorizon wavelength fluctuations and a second field that carries fluctuations at the observed scales. Gradients in the modulation field naturally pick out a preferred direction within our horizon. Such models have been proposed to explain both the hemisphere asymmetry [2, 12, 18] and the quadrupole-octopole alignment [17].

The structure of the paper is as follows. In § II we discuss the general form of the modulation model and develop the simulation tools to predict the polarization field. The analytic framework for polarization predictions and explicit relations for the simplest modulation statistics are given in the Appendix. In § III, we study the polarization predictions for the dipolar modulation models that are designed to explain the hemisphere asymmetry. We continue in § IV by studying quadrupolar modulation models that explain the quadrupole-octopole alignment. We discuss our results in § V.

*Hubble Fellow
†Electronic address: cdvorkin@uchicago.edu

II. SPONTANEOUS ISOTROPY BREAKING

A. Modulation Model

We consider a model where a superhorizon scale modulation of the gravitational potential field causes the CMB temperature field to locally look statistically anisotropic, even though globally the model preserves statistical homogeneity and isotropy. We generalize the considerations of Gordon *et al.* [17] by explicitly working with a 3D model of the gravitational potential as required for a polarization analysis.

Let us begin by assuming that the source of gravitational potential or curvature fluctuations depends on the product of two fields $g(\mathbf{x})$ and $h(\mathbf{x})$. For example, these curvature fluctuations might arise from an inflaton decay rate that depended on two fields, each with their own quantum fluctuations. Let us further assume that the field $h(\mathbf{x})$ has only superhorizon scale fluctuations so that in any given Hubble volume, it takes on a deterministic value whereas $g(\mathbf{x})$ has subhorizon scale power that appears as stochastic fluctuations within the volume.

Within our Hubble volume, an observer would see broken statistical homogeneity from the slow modulation of $h(\mathbf{x})$ across the volume. Furthermore, the local gradient and curvature of $h(\mathbf{x})$ naturally picks out a direction and breaks statistical isotropy as well. This broken isotropy is then transferred to the CMB through the Sachs-Wolfe effect [19] for the temperature field and Thomson scattering during reionization for the polarization field. Nonetheless, a full spatial average over many Hubble volumes would show no statistical inhomogeneity or anisotropy.

To make these considerations compatible with the observed statistical homogeneity and isotropy on small scales, we add another field that is responsible for fluctuations well below the horizon scale. Specifically, we model the Newtonian curvature fluctuation as

$$\Phi(\mathbf{x}) = g_1(\mathbf{x})\,[1+h(\mathbf{x})] + g_2(\mathbf{x})\,, \tag{1}$$

where $g_1(\mathbf{x})$ and $g_2(\mathbf{x})$ are Gaussian random fields and $h(\mathbf{x})$ is the modulating long-wavelength field. We will refer to the latter as the "modulating field" throughout this work.

Several important properties of this model are revealed in Fourier space. The product of fields in physical space becomes a convolution in Fourier space

$$\Phi(\mathbf{k}) = g_1(\mathbf{k}) + \int \frac{d^3k'}{(2\pi)^3} g_1(\mathbf{k}')h(\mathbf{k}-\mathbf{k}') + g_2(\mathbf{k})\,. \tag{2}$$

Two point correlations in g_1 and g_2 are determined by their respective power spectra

$$\begin{aligned}\langle g_1^*(\mathbf{k})g_1(\mathbf{k}')\rangle &= (2\pi)^3\delta(\mathbf{k}-\mathbf{k}')P_{g_1}(k)\,,\\ \langle g_2^*(\mathbf{k})g_2(\mathbf{k}')\rangle &= (2\pi)^3\delta(\mathbf{k}-\mathbf{k}')P_{g_2}(k)\,.\end{aligned} \tag{3}$$

We will typically assume that g_1 has power in fluctuations near the horizon scale and g_2 has power on subhorizon scales. The modulating field h has only superhorizon modes. That the two point correlations do not couple modes of different $\mathbf{k}$ is a consequence of statistical homogeneity and that the power spectrum is a function of $k=|\mathbf{k}|$ only is a consequence of statistical isotropy.

Notice that in the presence of the modulation h, Φ does not obey statistical homogeneity and isotropy

$$\begin{aligned}\langle\Phi^*(\mathbf{k})\Phi(\mathbf{k}')\rangle &= (2\pi)^3\delta(\mathbf{k}-\mathbf{k}')[P_{g_1}(k)+P_{g_2}(k)]\\ &\quad +[P_{g_1}(k)+P_{g_1}(k')]h(\mathbf{k}'-\mathbf{k})\\ &\quad +\int\frac{d^3\tilde{k}}{(2\pi)^3}P_{g_1}(\tilde{k})h^*(\mathbf{k}-\tilde{\mathbf{k}})h(\mathbf{k}'-\tilde{\mathbf{k}})\,,\end{aligned} \tag{4}$$

where the ensemble average is over realizations of g_1 and g_2 only. In particular, $\mathbf{k}$ modes that are separated by less than the horizon wavenumber are correlated and their amplitude depends on the direction of $\mathbf{k}$ despite the statistical isotropy of g_1.

B. Temperature Field

Broken homogeneity and isotropy are transferred onto the CMB temperature field through the Sachs-Wolfe effect. Horizon scale fluctuations in the Newtonian curvature at recombination imprint large scale temperature perturbations as

$$\frac{\Delta T}{T}(\mathbf{x}) = -\frac{1}{3}\Phi(\mathbf{x})\,. \tag{5}$$

To the observer at the origin, temperature inhomogeneities on a shell at the distance $D_{\rm rec}$ that a photon travels since recombination appear as anisotropies in a direction $\hat{\mathbf{n}}$

$$\frac{\Delta T}{T}(\hat{\mathbf{n}}) = \frac{\Delta T}{T}(\mathbf{x}=D_{\rm rec}\hat{\mathbf{n}})\,. \tag{6}$$

The analogue of a Fourier decomposition for the potential field is the spherical harmonic decomposition of the temperature field

$$\frac{\Delta T}{T}(\hat{\mathbf{n}}) = \sum_\ell\sum_{m=-\ell}^{\ell} T_{\ell m}Y_{\ell m}(\hat{\mathbf{n}})\,, \tag{7}$$

where $Y_{\ell m}$ are spherical harmonics.

Given a statistically homogeneous and isotropic potential field, the two point correlations in the temperature field obey

$$\langle T^*_{\ell' m'}T_{\ell m}\rangle = C_\ell^{TT}\delta_{\ell\ell'}\delta_{mm'}\,, \tag{8}$$

where C_ℓ^{TT} is the angular power spectrum of the temperature field. In the presence of the modulating field, the properties of the two point correlation of the potential in Eq. (4) carry over to the temperature field: modes of neighboring ℓ are correlated and the power depends on direction, *i.e.* the value of m.

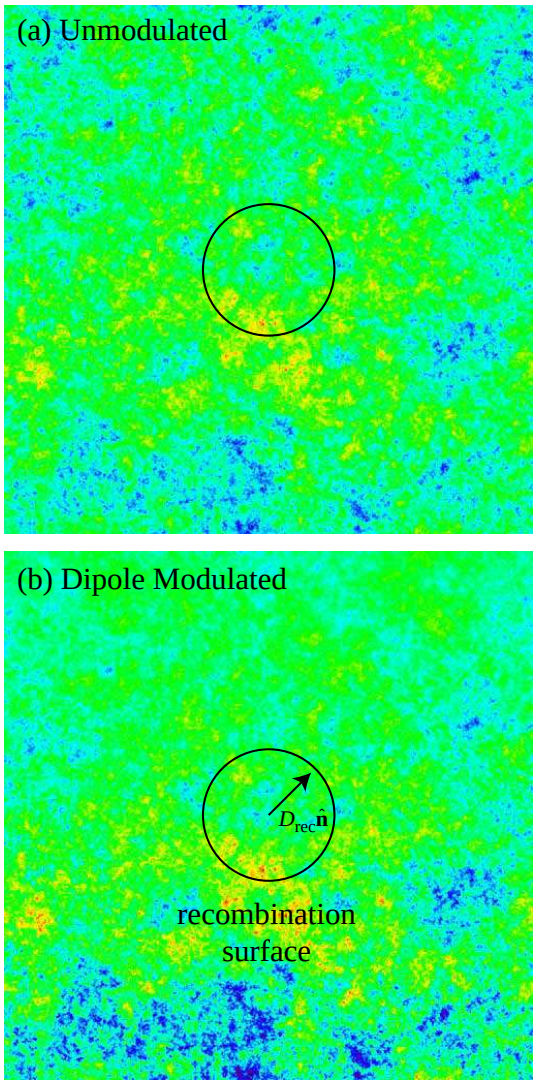

FIG. 1: Simulations of modulated temperature field. (a) Gaussian random unmodulated field g_1. (b) Dipole modulated potential field with $h(\mathbf{x}) = w_1\sqrt{3/4\pi}(z/D_{\rm rec})$ where the z axis is the modulation axis. Also shown (circle) is the surface at recombination upon which the observed temperature field originates. Note the power asymmetry in the modulated field.

The two point correlation of the model in terms of the power spectra of the fields g and h was given in [17] and is rederived in our framework of 3D fields in §A 1. In this framework, the modulation appears as the product of the Gaussian random field $g_1(\mathbf{x})$ and the modulation field $h(\mathbf{x})$ to form the observed temperature field. For the temperature field, this is equivalent to the product of the 2D angular fields projected onto the recombination surface (see Fig. 1, solid circle). Likewise the two point correlation can be expressed in terms of operations on the angular power spectra of the g and h fields in projection. We shall now see that these simplifications do not carry over to the polarization field.

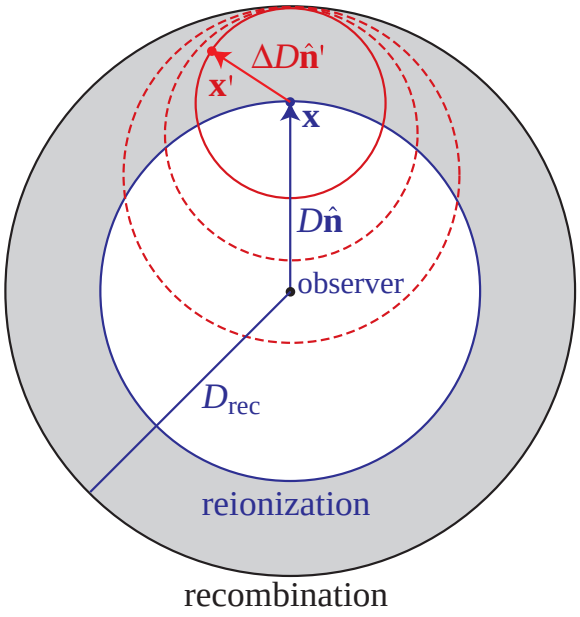

FIG. 2: Schematic diagram for polarization generation. After reionization, free electrons along the line of sight $\hat{\mathbf{n}}$ at a position $\mathbf{x}$ see a quadrupole anisotropy on their recombination surfaces at a distance ΔD in their angular coordinates $\hat{\mathbf{n}}'$. Thomson scattering off these electrons produces the polarization field viewed by the observer at the origin in direction $\hat{\mathbf{n}}$.

C. Polarization Field

Broken homogeneity and isotropy are also transferred onto the CMB polarization field. A modulation model that is designed to explain temperature anomalies can be tested through the predictions it makes for polarization.

Large-angle polarization is generated by the rescattering of photons off free electrons during the reionization epoch. A quadrupole anisotropy in the temperature of the radiation leads to linear polarization of the CMB. More specifically, from the temperature field at recombination of Eq. (5), the quadrupole moments at each position in space are given by

$$T_{2m}(\mathbf{x}) = \int d\hat{\mathbf{n}}' Y^*_{2m}(\hat{\mathbf{n}}')\frac{\Delta T}{T}(\mathbf{x}')\,. \qquad (9)$$

Note that T_{2m} describes a set of 5 three dimensional source fields. Furthermore the angular integral is over the recombination surface of an (electron) observer at position $\mathbf{x}$ a distance D away from the true observer at the origin

$$\mathbf{x}' = \mathbf{x} + \Delta D\hat{\mathbf{n}}'\,, \qquad (10)$$

where $\Delta D = D_{\rm rec} - D$ is the radius of recombination surface of the electron, as illustrated by Fig. 2.

To the true observer at the origin, scattering at position $\mathbf{x} = D\hat{\mathbf{n}}$ generates a contribution to the Stokes

parameters of the polarization in direction $\hat{\mathbf{n}}$ given by [20]

$$(Q \pm iU)(\hat{\mathbf{n}}) = -\frac{\sqrt{6}}{10}\int dD \frac{d\tau}{dD} e^{-\tau(D)} \times \sum_{m=-2}^{2} T_{2m}(D\hat{\mathbf{n}})_{\pm 2}Y_{2m}(\hat{\mathbf{n}}), \quad (11)$$

where ${}_{\pm 2}Y_{\ell m}$ are the spin ± 2 spherical harmonics and $\tau(D)$ is the optical depth between a comoving distance D and the present epoch. When we specify τ without the argument D, we refer to the total optical depth to reionization. The analogue of temperature multipole moments $T_{\ell m}$ for linear polarization are the $E_{\ell m}$ and $B_{\ell m}$ multipole moments

$$(Q \pm iU)(\hat{\mathbf{n}}) = -\sum_{\ell m} [E_{\ell m} \pm iB_{\ell m}]\, {}_{\pm 2}Y_{\ell m}(\hat{\mathbf{n}}). \quad (12)$$

E and B modes are the tensor analogues of curl-free and divergence free components of a vector. An E-mode has a polarization direction that is aligned with or orthogonal to the direction that the mode amplitude changes. A B-mode has this direction rotated by $\pm 45°$. When polarization is generated by a scalar field, only E-modes are formed. In Fourier space, this property is easily seen since the polarization direction from each $\mathbf{k}$ mode must follow the direction of $\hat{\mathbf{k}}$ itself. Since the modulation preserves the scalar nature of the source of polarization, B-modes are absent even in the modulated case. Note that this is different from a direct modulation of the polarization amplitude itself by a scalar quantity, e.g. from spatial fluctuations in τ [20]. In that case, the polarization direction is fixed by the potential field from recombination but the amplitude carries additional directionality from the modulation.

Predictions for the modulated polarization field, unlike the temperature field, require a 3D model of the modulation. Eq. (10) implies that the relevant modulation is at position $\mathbf{x}'$ in a sphere around each source at position $\mathbf{x} = D\hat{\mathbf{n}}$ for each angular position $\hat{\mathbf{n}}$ (see Fig. 2). Furthermore, these sources lie in the interior of the recombination surface $D < D_{\rm rec}$ of the temperature field. Likewise the polarization statistics cannot be expressed as an operation on the angular power spectra of the fundamental g and h fields corresponding to a single projection. The analytic framework for predicting the two point correlations is given in §A 2. Given the cumbersome nature of this framework, we instead rely on numerical simulations to study modulated statistics as we shall now describe. We use the analytic framework to test these simulations (see §A 3) and to provide insight on statistical quantities that should be measured in the simulations and data (see §A 4).

D. Simulations

Numerical simulations are conceptually the simplest and most general way of assessing the statistics of the modulated temperature and polarization fields.

We first simulate the 3D potential field $\Phi(\mathbf{x})$ by combining realizations of the two Gaussian random g-fields with the deterministic modulation field h. We typically chose the length of the periodic box to be four times the diameter of the recombination surface with 512^3 pixels. This ratio of sizes and dynamic range allows us to cover the $2 \leq \ell \lesssim 10$ scales of interest in this work.

To obtain the temperature field, we then interpolate the field onto a 2D surface of radius $D_{\rm rec}$ and weight it according to the Sachs-Wolfe relation (5). Finally we use the HEALPix package [21] to extract the multipole moments of the field. The interpolation is done in every unit vector $\hat{\mathbf{n}}$ corresponding to $12,288$ HEALPIX pixel centers at resolution $N_{\rm side} = 32$. As an example, slices through simulations of unmodulated and dipole-modulated temperature fields are shown in Fig. 1. The statistics of these temperature simulations match those of the 2D approach where the modulation is directly in angular space on the recombination surface. We will occasionally use 2D simulations where only the temperature field is required and for unmodulated cases to build large samples.

The polarization field is equally straightforward to simulate but numerically more involved. We take the same 3D simulations employed for the temperature field and compute the quadrupolar temperature sources for 80 redshifts in equal steps along each line of sight, and in every unit vector $\hat{\mathbf{n}}$ corresponding to $12,288$ HEALPIX pixel centers at resolution $N_{\rm side} = 32$ around the sky. Then, we generate maps of polarization by means of Eq. (11). Once the maps are created, the coefficients $E_{\ell m}$ are obtained using the HEALPix package [21], and various polarization statistics described below are computed.

We test this pipeline against analytic calculations of unmodulated and simple modulation models in §A 3. It is the main tool used to assess the temperature and polarization statistics in this work. It can be used for arbitrarily complicated modulation fields and any statistical property of the temperature and polarization fields.

III. DIPOLAR MODULATION

Eriksen *et al.* [5] showed that there is a hemispherical or dipole asymmetry in the amount of power in the WMAP data at multipoles $\ell \sim 20 - 40$. The axis of this asymmetry points in a direction that is close to the South Ecliptic Pole (SEP) making the power in the southern hemisphere larger than the north. It was subsequently pointed out that a dipolar modulation of the form of Eq. (A1) with a modulation field of

$$h(x) = w_1 Y_{10}\left(\frac{z}{D_{\rm rec}}\right), \quad (13)$$

could explain the asymmetry though not the curious alignment with the SEP [2, 12, 18]. Note that $Y_{10}(z/D_{\rm rec}) = \sqrt{3/4\pi}(z/D_{\rm rec})$ in a coordinate system where the z-axis points along the modulation axis. We set the g_2 field to have power only at $\ell > 40$ and hence its contribution is irrelevant in our considerations. We take the g_1 field to have a scale invariant power spectrum

$$\frac{k^3 P_{g_1}(k)}{2\pi^2} = \frac{9}{25}\delta_\zeta^2 \tag{14}$$

with $\delta_\zeta = 4.6\times10^{-5}$ which corresponds to the WMAP 3-year normalization for a cosmology with matter density $\Omega_m = 0.24$, cosmological constant $\Omega_\Lambda = 0.76$, baryon density $\Omega_b h^2 = 0.022$, Hubble constant $H_0 = 73$ km s^{-1}, and spatially flat spatial geometry.

Once w_1 is specified, we can use our simulation pipeline to make realizations of the polarization field. An extreme example with $w_1 = 2.5$ is shown in Fig. 3. Note that the hemispherical power asymmetry carries through to the polarization. The WMAP temperature field however

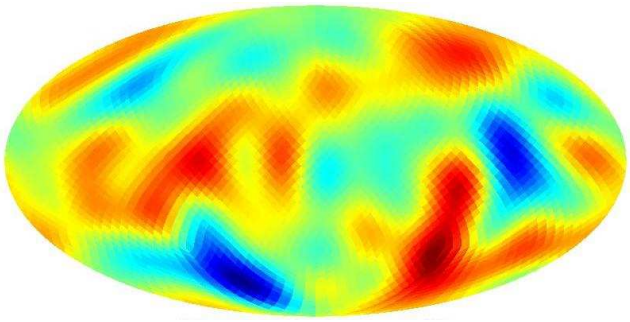

FIG. 3: Map composed of the first 10 multipoles of the E polarization field in a dipole modulation model with $w_1 = 2.5$. The power is larger in the southern hemisphere.

suggests a much weaker dipole modulation that can only be detected statistically in the polarization. We will base our parameter choices on the analysis of Ref. [12] which found $w_1 = 0.23 \pm 0.07$ with $w_1 = 0$ excluded at the 99% CL. For illustrative purposes we will take a reionization model with $\tau = 0.09$ where hydrogen is fully ionized out to a maximum redshift and neutral thereafter. We test sensitivity to the reionization history in §III B.

A. Dipole Modulation Statistics

The dipolar modulation in the potential field gives rise to couplings between ℓ and $\ell' = \ell \pm 1$ multipole moments in not only TT

$$\langle T^*_{\ell m} T_{\ell+1,m}\rangle \propto w_1\,, \tag{15}$$

but also in all of the two point combinations involving E

$$\langle X^*_{\ell m} Y_{\ell+1,m}\rangle \propto w_1\,, \tag{16}$$

specifically $XY \in \{TE, ET, EE\}$. We derive the proportionality coefficients in Appendix A 4. Each multipole pair then forms a noisy estimator of the dipole modulation parameter w_1. Even in the absence of detector noise and foregrounds, the cosmic variance of the temperature and polarization fields provide noise to the measurement. Eqs. (A39) and (A40) give the unbiased minimum variance combinations of the multipole pairs as estimators of w_1.

The first question we ask is: if the observed dipole asymmetry at $\ell \sim 20-40$ is a statistical fluke and that the true ensemble average is $w_1 = 0$, how well can temperature and polarization at $\ell \lesssim 10$ rule out a finite value of w_1 near the best fit of $w_1 \approx 0.2$? Under this assumption, we show the distribution of the XY estimators and the joint estimator in Fig. 4. These distributions were generated from 10^5 2D simulations of the unmodulated temperature and polarization fields in accordance with the power spectra of Eq. (A9), (A20) and (A30).

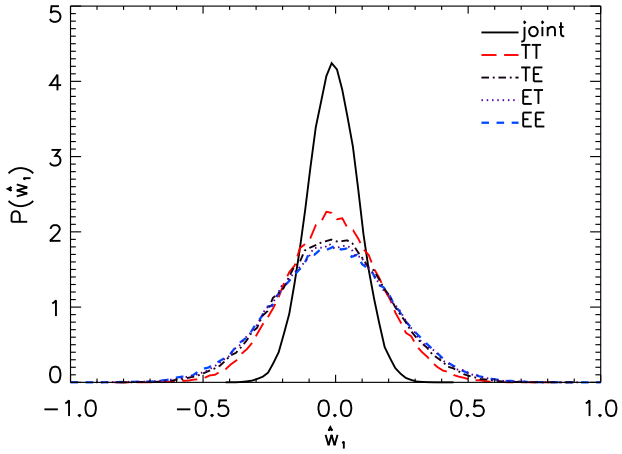

FIG. 4: Probability distribution of the dipole modulation estimators $\hat{w}_1^{XY}$ for a model with $w_1 = 0$ where XY represents the two fields whose ℓ and $\ell+1$ multipoles are correlated: TT (red long-dashed curve), TE (black dotted-dashed curve), ET (violet dotted curve) and EE (blue thick dashed curve). The minimum variance joint estimator $\hat{w}_1$ is shown as the solid curve. We have assumed cosmic variance limited measurements and $\ell_{\rm max} = 11$ for all estimators.

Given TT alone, the hypothesis that $w_1 \sim 0.2$ can only be weakly tested. Specifically, a value of $w_1 \geq 0.2$ can be tested at the 86.4% confidence level (CL) by TT. Each of the polarization estimators can in principle test dipole modulation at a comparable level: $w_1 \geq 0.2$ can be tested at 81.6% confidence by EE, at 83.4% CL by TE and at 82.1% CL by ET. The combination of the four estimators however is more powerful: $w_1 \geq 0.2$ can be tested at 98.4% CL by the joint estimator. For reference, the central value of [12], $w_1 = 0.23$, yields a 99.3% CL test. Furthermore the 95% upper limit on w_1 achievable with the joint estimator is $w_1 \leq 0.15$.

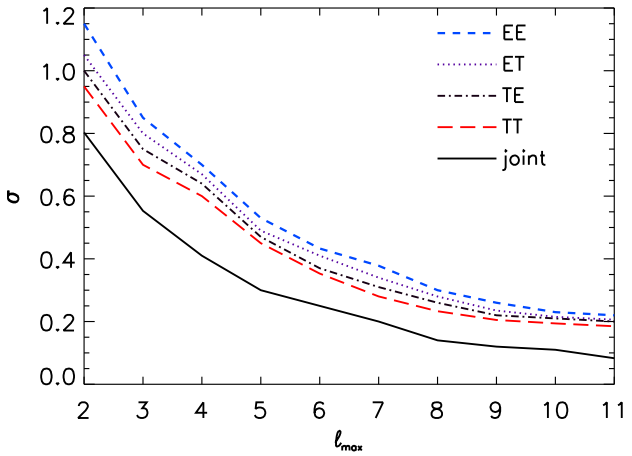

FIG. 5: Standard deviation of the individual estimators $\hat{w}_1^{XY}$ and the joint estimator (black) as a function of maximum multipole pair employed in the estimators $\ell_{\rm max}$. The individual XY pairs are TT (red long-dashed curve), TE (black dotted-dashed curve), ET (violet dotted curve) and EE (blue dashed curve) from the analytic calculation of the Appendix.

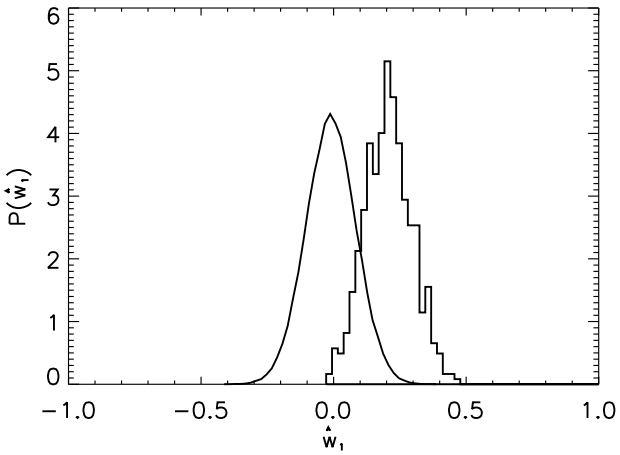

FIG. 6: Histogram of the joint estimator $\hat{w}_1$ coming from 545 3D realization of the dipole modulation model with $w_1 = 0.2$ and $\tau = 0.09$. For comparison, the probability distribution for the isotropic $w_1 = 0$ model from Fig. 4 is also plotted (smooth curve).

Most of the polarization information comes from multipoles in the range of $\ell \sim 4-8$. In Fig. 5 we show the rms fluctuation in the estimators as a function of $\ell_{\rm max}$, the maximum multipole employed in the estimators. Note that the estimators involving polarization saturate by $\ell \sim 10$.

The next question we ask is: given a true model of $w_1 = 0.2$, how well can an isotropic model of $w_1 = 0$ be excluded? Fig. 6 shows the distribution of w_1 coming from 545 realizations of a 3D modulated model (histogram, $\ell_{\rm max} = 11$). In these simulations $w_1 \leq 0$ occurred in less than 1% of the realizations. Furthermore the mean of the samples $\langle \hat{w}_1 \rangle = 0.20$ is consistent with being unbiased and the standard deviation $\sigma = 0.08$ is consistent with the expectations from Fig. 5.

B. Model Dependence and Noise

These tests are only weakly sensitive to the assumed reionization history for a cosmic variance limited observation. The main difference is that a linear modulation produces a weaker effect for nearby sources of polarization and hence the signal decreases with τ. As an example, we calculate the level of detectability for an unphysically small optical depth of $\tau = 0.0279$. Even for this extreme case, values of $w_1 \geq 0.2$ are ruled out at the 96.4% CL by the joint estimator. An intermediate case of $\tau = 0.055$ rules out values of $w_1 \geq 0.2$ at the 98% CL.

Because most of the signal comes from low multipoles in the polarization $\ell \sim 4 - 8$, the cosmic variance limit described in the previous section is within the statistical reach of the Planck satellite. For definiteness we take the 143 GHz and 217 GHz frequency channels and combine them into an effective white noise power spectrum of $N_\ell^{EE} = (67.6\mu\text{K-arcmin})^2$ at low multipoles. Noise in the temperature field is negligible compared with cosmic variance. Quantitatively, for a reionization history with optical depth $\tau = 0.09$, and the noise level considered for Planck, values of $w_1 \geq 0.2$ are ruled out at 97.8% CL by the joint estimator $\hat{w}_1$. A space-based experiment with no foregrounds, 5 frequency channels and a noise level of 18μK-arcmin per frequency channel would essentially saturate the cosmic variance bound in each channel. Given these results, foregrounds and systematics will probably be the limiting factor in how well dipole modulation can be tested by polarization. We leave this subject to a future work.

Finally, the model spectrum assumes that the temperature anisotropy comes purely from the Sachs-Wolfe effect. A ΛCDM model would predict that the ensemble averaged quadrupole has a substantial contribution from the so-called Integrated Sachs-Wolfe (ISW) effect from the decay of potentials during the acceleration epoch. Under ΛCDM, the measured low power quadrupole anisotropy could indicate that either the ISW contributions to the quadrupole are by chance small on our sky or that there is a chance cancellation between the two contributions. Finally, it could indicate an alternate model of the dark energy where the ISW contributions are smaller [22, 23, 24] or designed to cancel the Sachs-Wolfe effect [25]. In all of these explanations, the polarization field is unaffected.

Nonetheless, the dipole modulation tests involving the temperature field are slightly weakened if the ISW contributions to ΛCDM are added back as a source of noise. Correspondingly the joint estimators also weaken. For example, for a reionization model with optical depth

$\tau = 0.09$ the joint estimator can test values of $w_1 \geq 0.2$ at the 97.6% CL.

In summary, prospects for future polarization tests of dipole modulation at the $w_1 \approx 0.2$ level at the $\sim$98% CL are fairly robust to model assumptions.

IV. QUADRUPOLAR MODULATION

de Oliveira-Costa *et al.* [7] pointed out that there are several striking features of the temperature dipole, quadrupole and octopole in the WMAP data. The octopole is highly planar and defines a preferred axis that is near the dipole axis. Moreover the quadrupole is also weakly planar in the same coordinate system.

Gordon *et al.* [17] subsequently showed that a quadrupolar modulation with a preferred axis that is by chance near the dipole direction can make these features substantially more likely. Specifically, we will take a modulation to the potential field of the form of Eq. (1), with

$$h(\mathbf{x}) = w_2 Y_{20}(\frac{z}{D_{\rm rec}})\,. \tag{17}$$

Note that the z-axis required here is *not* the same as in the dipole modulation case. Since $Y_{20}(z/D_{\rm rec}) = (1/4)\sqrt{5/\pi}\left[3(z/D_{\rm rec})^2 - 1\right]$, this introduces a quadratic term to the spatial modulation.

These anomalies are confined to the low multipoles and so the modulation must also be confined to low multipoles. For the angular modulation considered in [17], this was simply imposed as a sharp suppression in multipole space of the g_1 field. Spatial modulation is more complicated in that even a sharp suppression in Fourier space is broadened by projection effects. Given these considerations, we take a two field model defined by

$$\frac{k^3 P_{g_1}(k)}{2\pi^2} = \frac{9}{25}\delta_\zeta^2 f^2, \qquad k_1 < k < k_2\,, \tag{18}$$

$$\frac{k^3 P_{g_2}(k)}{2\pi^2} = \frac{9}{25}\delta_\zeta^2, \qquad k > k_3\,, \tag{19}$$

where the normalization δ_ζ is given as in the dipole modulation model by the WMAP normalization. We introduce a scaling parameter f that controls the amount of power at low k relative to this normalization. We begin our analysis by finding regions in the parameter space of $\{w_2, k_1, k_2, k_3, f\}$ that maximize the probability of the observed quadrupole-octopole alignment.

A. Maximizing Temperature Alignments

To quantify the quadrupole-octopole alignment, de Oliveira-Costa *et al.* [7] introduced the normalized angular momentum along a given axis (θ, ϕ)

$$\hat{L}_\ell^2(\theta,\phi) = \frac{\sum_m m^2 |T'_{\ell m}|^2}{\ell^2 \sum_m |T'_{\ell m}|^2}\,, \tag{20}$$

where the $T'_{\ell m}$ are the multipole moments of the temperature field in that preferred frame. More specifically, from the moments defined in galactic coordinates $T_{\ell m}$, the rotated ones are

$$T'_{\ell m'} = \sum_m T_{\ell m} D^\ell_{m m'}(-\psi, -\theta, -\phi)\,, \tag{21}$$

where the Euler angles are $\psi \in [0, 2\pi]$, $\theta \in [0, \pi]$, and $\phi \in [0, 2\pi]$ and $D^\ell_{m m'}(-\psi, -\theta, -\phi)$ is the Wigner rotation matrix [8, 17]. Note that $\hat{L}_\ell^2$ is invariant under the final rotation by ψ.

In particular, the statistic

$$\hat{L}_{23}^2 = \frac{1}{2}(\hat{L}_2^2 + \hat{L}_3^2)\,, \tag{22}$$

captures both the alignment between the quadrupole and octopole, and the planarity of the octopole. The preferred axis is then chosen as the one which maximizes this statistic. For the ILC map of the 3-year WMAP data corrected for the kinematic quadrupole, $\hat{L}_{23}^2 = 0.943$. This is slightly smaller than for the 1-year WMAP data in the TOH map [9], used in previous studies: $\hat{L}_{23}^2 = 0.96$ [8, 17]. For an unmodulated model, $\hat{L}_{23}^2 \geq 0.943$ occurred in only 0.85% of 10^4 2D realizations.

Quadrupole modulation can dramatically increase the probability of a high angular momentum statistic. To find the parameters that maximize this probability, we first vary the parameters $\{w_2, k_1, k_2\}$ with $k_3 \to \infty$ and find the set that gives maximum number of realizations with $\hat{L}_{23}^2 > 0.943$. Taking $k_3 \to \infty$ eliminates the contributions from the unmodulated g_2 field that could otherwise destroy alignments at low multipoles. The alignment probability then is also independent of f.

We then generate 10^4 2D Monte Carlo (MC) realizations for each of the modulated models. For each realization, the estimator $\hat{L}_{23}^2$ is computed on a grid of 10^8 positions on the celestial sphere by performing the rotation of $T_{\ell m}$ in Eq. (21). Taking the maximum value of $\hat{L}_{23}^2$ attained for each realization, we compute for each model the percentage of realizations with $\hat{L}_{23}^2 > 0.943$.

The region of parameter space that corresponds to the highest alignments is centered around $w_2 \approx -7$, in agreement with [17]. Furthermore, wavenumbers that best project onto a multipole ℓ correspond to $kD_{\rm rec} \sim \ell$; more specifically $kD_{\rm rec} \approx 4.2$ for the region that best projects onto the quadrupole and octopole at the distance to recombination. Furthermore keeping k_1 and k_2 in a narrow range around this value eliminates contamination from the modulation of longer and shorter wavelengths in the quadrupole and octopole.

For definiteness, we take $w_2 = -7$, $k_1 D_{\rm rec} = 4.2$ and $k_2 D_{\rm rec} = 4.23$ though any $(k_2 - k_1) D_{\rm rec} \lesssim 0.05$ would produce similar results due to unavoidable projection effects. With this choice, 21.8% of realizations have $\hat{L}_{23}^2 > 0.943$. This number is smaller than that quoted in [17] due to these projection effects but is still a factor of 25.6 larger than the probability in unmodulated models.

While taking $k_3 \to \infty$ maximizes alignments, it does not provide for a realistic model. The absence of high wavenumbers would be in conflict with the observed fluctuations at higher multipole moments. This is exhibited in a poor ILC likelihood

$$\mathcal{L}(\mathbf{T}|\mathbf{C}) = \frac{1}{(2\pi)^{N/2}\sqrt{\det \mathbf{C}}} \exp[-\frac{1}{2}\mathbf{T}^\dagger \mathbf{C}^{-1}\mathbf{T}]\,, \qquad (23)$$

where $\mathbf{T}$ is the N element vector of observed $T_{\ell m}$ values and $\mathbf{C}$ is their signal plus noise covariance matrix. To remedy this problem we keep the first field fixed to the parameters above but add in the second field at a finite k_3 and maximize the likelihood over their relative amplitude f.

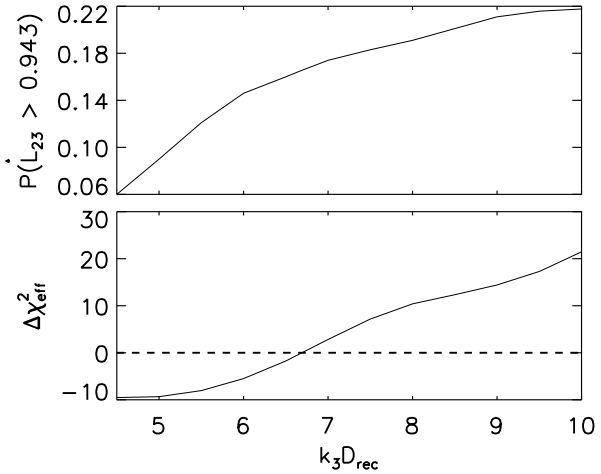

FIG. 7: Effect of the unmodulated field on alignments and goodness of fit of quadrupole modulation models. The upper panel shows the fraction of realizations that have a higher angular momentum statistic $\hat{L}^2_{23}$ than WMAP 3-year ILC as a function of $k_3 D_{\rm rec}$ which controls the contribution of the unmodulated field to the low multipoles. The dependence of $\Delta\chi^2_{\rm eff}$ (relative to ΛCDM, dashed line) is shown in the lower panel.

Fig. 7 (lower panel) shows the dependence of $\chi^2_{\rm eff} \equiv -2\ln\mathcal{L}$ on $k_3 D_{\rm rec}$ for $\ell = 2-5$ relative to ΛCDM (see below Eq. (14)). Decreasing this parameter creates a better fit to the data at the expense of decreasing the probability of the quadrupole-octopole alignment (upper panel). As a compromise we choose a model with $\Delta\chi^2_{\rm eff} = 0$ that neither improves nor worsens the fit. The model parameters then become

$$k_1 D_{\rm rec} = 4.2\,, \quad k_2 D_{\rm rec} = 4.23\,, \quad k_3 D_{\rm rec} = 6.697\,,$$
$$w_2 = -7\,, \quad f = 5.77\,, \quad \tau = 0.09\,, \qquad (24)$$

for which the probability of $\hat{L}^2_{23} > 0.943$ is 16.6% (see Fig. 8).

Fig. 9 shows the temperature angular power spectrum of this model along with the WMAP 3-year temperature data for the first 10 multipoles. The bands shown here represent the 68% and 95% cosmic variance confidence regions for this model taken from 10^4 2D realizations of the temperature field. Note that the cosmic variance is larger for the modulated model due to the m-dependence of the power.

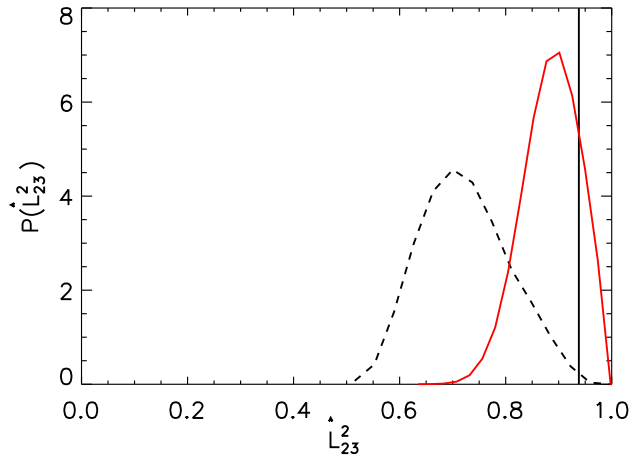

FIG. 8: Distribution of $\hat{L}^2_{23}$ (red solid line) for the quadrupolar modulation model of Eq. (24). 16.6% of the 10^4 realizations of this model have $\hat{L}^2_{23} > 0.943$. The distribution for the isotropic case is shown as a dashed line for comparison, where 0.85% have $\hat{L}^2_{23}$ larger than the WMAP ILC value: 0.943 (vertical line).

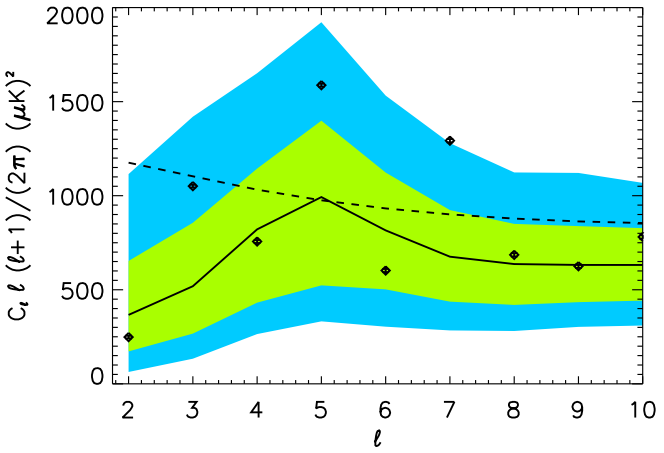

FIG. 9: Temperature angular power spectrum of the quadrupolar modulation model of Eq. (24) (solid line). The WMAP ILC data with noise errors are also shown. The solid bands correspond to the 68% and 95% cosmic variance confidence regions of the model. The dashed line represents the ΛCDM model against which this model is compared in Fig. 7.

In Fig. 10 we show a realization of the model that has a high normalized angular momentum $\hat{L}^2_{23} = 0.94$, shown in the frame of the modulation, illustrating how

the modulation takes a random isotropic sky and aligns the quadrupole and the octopole.

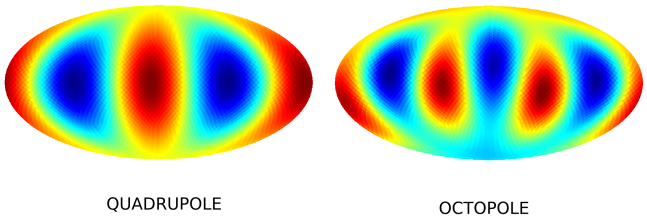

FIG. 10: Quadrupole and octopole of the temperature field from one realization of the quadrupole modulation model of Eq. (24). The normalized angular momentum here is $\hat{L}^2_{23} = 0.94$. The range goes from -50μK to 50μK for both cases.

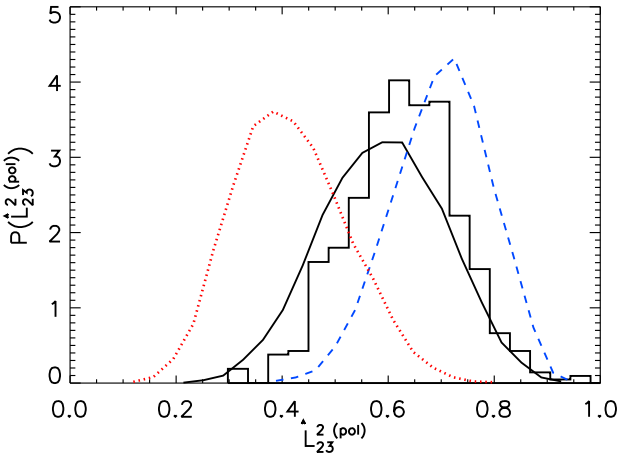

FIG. 11: Histogram of $\hat{L}^{2(\rm pol)}_{23}$ for 571 3D realizations of the quadrupole modulation model of Eq. (24) that also have $\hat{L}^2_{23} \geq 0.943$. For comparison we also show the distribution for isotropic random polarization fields (red dotted lines). Isotropic realizations constrained to the $T_{\ell m}$ values of the ILC map have a distribution shifted to higher alignment values given the temperature-polarization correlation with just the Sachs-Wolfe effect (blue dashed lines) and with ΛCDM ISW contributions added (black solid curve).

B. Polarization Angular Momentum

With the quadrupolar modulation model set by Eq. (24) to maximize temperature alignments and fit the WMAP temperature data, we can now use our simulations to make polarization predictions.

We first examine the normalized angular momentum statistic of the polarization field. We define this statistic in the same way as for the temperature field

$$\hat{L}^{2(\rm pol)}_l = \frac{\sum_m m^2 |E_{\ell m}|^2}{\ell^2 \sum_m |E_{\ell m}|^2}\,, \tag{25}$$

with the combined quadrupole and octopole statistic being

$$\hat{L}^{2(\rm pol)}_{23} = \frac{1}{2}(\hat{L}^{2(\rm pol)}_2 + \hat{L}^{2(\rm pol)}_3)\,. \tag{26}$$

There is one important difference between this statistic and the temperature based one. In the case of polarization predictions, the temperature field has already defined the preferred axis against which we should measure the polarization angular momentum. Consequently, no search over directions is required.

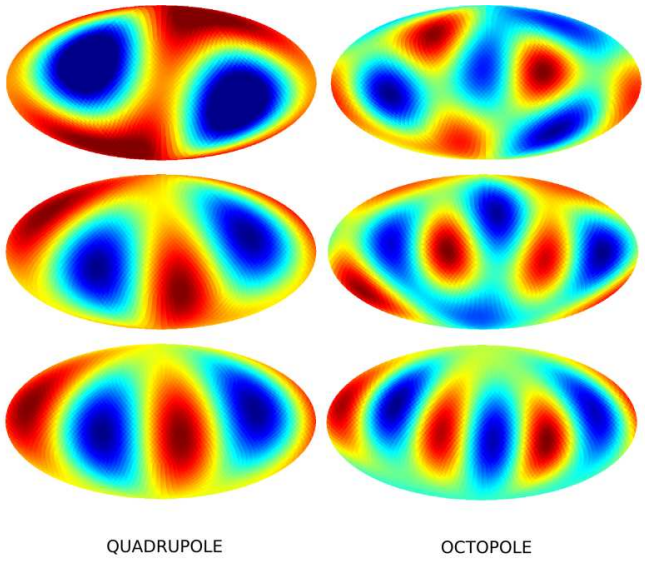

FIG. 12: Realizations of the quadrupole (left column) and octopole (right column) of the E component of the polarization field in order of increasing alignment: isotropic case with $\hat{L}^{2(\rm pol)}_{23} = 0.46$ (first row), quadrupolar modulation model with parameters given by Eq. (24) with $\hat{L}^{2(\rm pol)}_{23} = 0.67$ (second row) and an isotropic Sachs-Wolfe model constrained to match the WMAP ILC temperature multipoles with $\hat{L}^{2(\rm pol)}_{23} = 0.9$ (third row). The color scale goes from -0.3μK to 0.3μK in all panels.

Fig. 11 shows a histogram of $\hat{L}^{2(\rm pol)}_{23}$ for 571 out of 3482 3D realizations of the modulated model that have as high or higher temperature alignment than WMAP $\hat{L}^2_{23} > 0.943$. We first compare this with the same statistic for 10^5 2D isotropic realizations of an unmodulated polarization field (red dotted line). There is a tendency for the polarization field to be aligned compared with random isotropic realizations. An example of a typical realization is shown in Fig. 12 (second row) and is to be compared with a typical isotropic realization (first row). Note the similarity between temperature alignments and

E polarization aligments in Figs. 10 and 12. Both have a deficit of power near the poles in the frame of the modulation. However the polarization amplitude $(Q^2+U^2)^{1/2}$ is in fact the largest at the poles. In this direction, the electron scattering sees the planar quadrupole in the transverse plane and scatters it into a maximal polarization. Foregrounds which have high polarization where there is high intensity will not have this pattern.

However, the expected correlation between the temperature and polarization fields implies that there should be *some* tendency for polarization alignment in *any* explanation in which the alignment of the temperature field reflects contributions from the recombination surface, and not a foreground, secondary or systematic effect. This includes an isotropic unmodulated model in which the temperature alignment is a chance occurrence.

To quantify this tendency, we consider two isotropic models which have been conditioned to have $\hat{L}_{23}^2 = 0.943$ for the temperature field. More specifically, we draw a polarization field that is consistent with the observed temperature field $T_{\ell m}$ and model power spectra,

$$E_{\ell m} = \frac{C_\ell^{TE}}{C_\ell^{TT}} T_{\ell m} + \sqrt{C_\ell^{EE} - \frac{(C_\ell^{TE})^2}{C_\ell^{TT}}}\, n_{\ell m}\,, \qquad (27)$$

where $n_{\ell m}$ is a complex Gaussian variate of zero mean with $\langle n_{\ell m}^* n_{\ell m}\rangle = 1$ and $n_{\ell m}^* = (-1)^m n_{\ell,-m}$.

The first is the Sachs-Wolfe model where all of the temperature anisotropy arises from recombination. Under this assumption, the temperature alignments are a real feature of the recombination surface and the ISW effect in our local universe happens to be small in the quadrupole and octopole. Fig. 11 (blue dashed lines) shows the polarization statistic for 10^5 2D constrained realizations of this model. An example of a highly aligned realization is shown in Fig. 12 (third row).

Compared with the modulated model, there is an even *higher* probability of polarization alignment here. The reason is that in the former, the strength of the spatial modulation increases as the square of the distance. The closer distance to reionization implies a substantially weaker modulation of the polarization field as compared with the temperature field. Ironically, a very high value of $\hat{L}_{23}^{2(\rm pol)}$ would strongly disfavor the modulated model compared with the isotropic Sachs-Wolfe model. The 95% upper limit for the modulated model is $\hat{L}_{23}^{2(\rm pol)} = 0.77$.

It is also possible that the alignment of the quadrupole and octopole does not represent an aligned spatial configuration at all and is instead the result of a chance combination of the Sachs-Wolfe effect and ISW effects. These effects arise from very different physical scales but are seen in projection at the same angular scale. To illustrate this case, we draw 10^5 2D realizations of the ΛCDM model (see below Eq. (14)) that are similarly conditioned to have $\hat{L}_{23}^2 = 0.943$ for the temperature field. The histogram of the polarization statistic is shown in Fig. 11 (black solid curve). The presence of a temperature contribution that does not correlate with polarization shifts the distribution downwards and decreases the probability of polarization alignments. The distribution is still distinct from the truly random isotropic simulations (red dotted lines). The 95% lower limit on this model is $\hat{L}_{23}^{2(\rm pol)} \geq 0.39$.

The final possibility is that the temperature quadrupole and temperature field is nearly all local secondary anisotropy and that the Sachs-Wolfe effect is anomalously low (e.g. [26, 27]). The polarization distribution would then look like the truly random isotropic simulations (see Fig. 11, red dotted line). In this case, the polarization amplitude itself would also be anomalously low.

In summary, a very low value of $\hat{L}_{23}^{2(\rm pol)} \lesssim 0.4$ with a normal polarization amplitude would suggest that the origin of the temperature alignments is not cosmological. A very low value with suppressed polarization amplitude would imply a purely secondary origin to the temperature alignment. A very high value $\hat{L}_{23}^{2(\rm pol)} \gtrsim 0.8$ would rule out the modulated model and also imply that the ISW effect is nearly absent in the WMAP low multipoles.

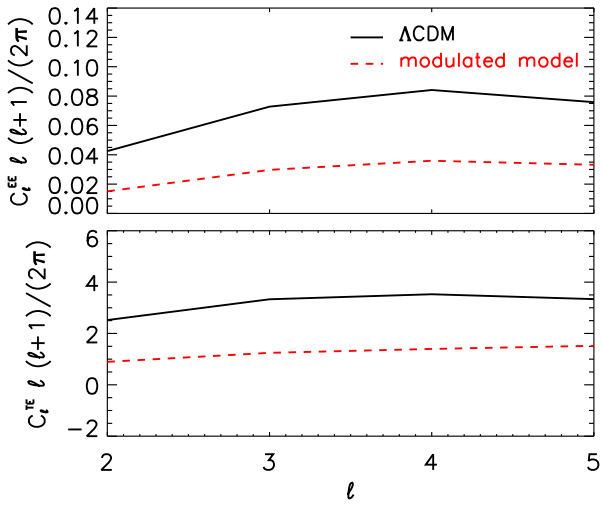

FIG. 13: EE and TE power spectra of the modulated model of Eq. (24) (red dashed lines) along with the ΛCDM power spectrum (black solid lines). The modulated model has a lower polarization at the same $\tau(= 0.09)$. The units are $(\mu\mathrm{K})^2$.

C. Quadrupole Modulation Statistics

Beyond the angular momentum of the quadrupole and octopole, a quadrupolar modulation model makes further testable predictions. These predictions however are more sensitive to the choice of model parameters.

First, the angular power spectrum of the polarization and temperature cross correlation differs in its relation-

ship to the temperature power spectrum due to the modulation. In Fig. 13, we show these spectra for the model of Eq. (24). Note that for the same optical depth τ, the polarization spectra have less power. This is a consequence of the decrease in modulation amplitude at the closer distance to reionization. Unfortunately, this signature is largely degenerate with a change in the optical depth and so is not a unique signature of modulation.

Similar to dipole modulation, quadrupole modulation generates a more unique signature in the correlation between neighboring multipole moments

$$\langle X^*_{\ell m} Y_{\ell+2,m}\rangle \neq 0\,, \tag{28}$$

where $XY \in \{TT, TE, ET, EE\}$. In our two field model, most of the modulation is confined to the low multipoles and so the signal is mainly in $\ell + 2 = 4, 5$. Note that an isotropic model that by chance has quadrupole-octopole temperature alignments will still predict a zero expectation value for these quantities.

Let us define a correlation statistic

$$\hat{s}^{XY}_{\ell m} = \frac{\mathrm{Re}(X^*_{\ell m} Y_{\ell+2,m})}{|X_{\ell m}||Y_{\ell+2,m}|}\,, \tag{29}$$

which tests the phase alignment of the moments and takes on values from $-1 \leq \hat{s}^{XY}_{\ell m} \leq 1$. In the absence of modulation, these statistics have zero mean but any given pair has large cosmic variance. Given a modulation model that predicts

$$s^{XY}_{\ell m,\mathrm{mod}} = \langle \hat{s}^{XY}_{\ell m}\rangle_{\mathrm{mod}}\,, \tag{30}$$

we can construct a weighted sum

$$\hat{s} = \frac{\sum_{\ell m, XY} s^{XY}_{\ell m,\mathrm{mod}} \hat{s}^{XY}_{\ell m}}{\sum_{\ell m, XY}\left(s^{XY}_{\ell m,\mathrm{mod}}\right)^2}\,, \tag{31}$$

where $\ell = 2, 3$. This statistic has the property that its expectation value is zero for an isotropic field and 1 for the chosen modulation model.

We begin by considering the $XY = TT$ case and the modulated model of Eq. (24) as in the previous section. The distribution of $\hat{s}$ is shown in Fig. 14 (dashed lines, right curve) from 10^5 2D simulations. The WMAP ILC data has $\hat{s} = 0.076$ and disfavors the modulated model but not at high significance: 3.5% of the modulated simulations have $\hat{s}$ less than the data. Conversely the data would be a typical realization of an isotropic model (see Fig. 14, dashed lines, left curve). Likewise an $\hat{s} \leq 0$ occurred in 2.5% of the modulated simulations, and an $\hat{s} \geq 1$ occurred in 2.3% of the isotropic simulations. These two tails of the respective distributions represent the power of the statistic to distinguish typical realizations of the models.

The addition of polarization information would make these tests definitive by reducing the probability in the tails (see Fig. 14, solid curves). When all fields are considered $XY \in \{TT, EE, TE, ET\}$, the probabilities in the tails drop to $\hat{s} \leq 0$ in only 0.09% of the 3482 modulated 3D simulations and $\hat{s} \geq 1$ in 0.24% of the 10^5 2D isotropic simulations. The latter probability assumes a Sachs-Wolfe only model for the temperature field. If the ISW contribution of ΛCDM is factored in, the probability increases slightly to 0.34%.

Consequently a quadrupolar modulation with parameters given by Eq. (24) will be definitively tested through the s statistic by polarization measurements that approach the cosmic variance limit for $\ell \leq 5$. However a model with a lesser amount of modulation at $\ell = 4, 5$ may evade such constraints. The amount of modulation in these multipoles is controlled by k_3 and hence $\hat{s}$ mainly constrains this parameter. In the model we have been considering, $k_3 D_{\mathrm{rec}} = 6.697$. Lowering this value increases the contribution of the unmodulated field for $\ell \leq 5$. But the price is to make the quadrupole-octopole alignment less likely (see Fig. 7).

As a specific example, for $k_3 D_{\mathrm{rec}} = 5.16$ and $f = 5.13$, the probability of $L^2_{23} > 0.943$ decreases from 16.6% to 10% (see Fig. 7). On the other hand, it improves the fit to the WMAP data by making $\Delta\chi^2_{\mathrm{eff}} = -9$ relative to ΛCDM. Correspondingly, the s-statistic also weakens in its discriminating power. For the TT case, the WMAP ILC data has $\hat{s} = 0.065$. For this case, 10.6% of 2521 simulations have a smaller value of $\hat{s}$. Similarly, a value of $\hat{s} \leq 0$ occurred in 9.1% of the modulated simulations, and $\hat{s} \geq 1$ occurred in 10.6% of the isotropic simulations. With the addition of polarization information these tests become more significant: $\hat{s} \leq 0$ only occurred in only 0.24% of the modulated simulations and $\hat{s} \geq 1$ only occurred in in 0.50% of the isotropic simulations.

In summary, while the s-statistic cannot rule out quadrupolar modulation in general, it can severely limit the amount of modulation allowable at $\ell \leq 5$ and hence test its ability to explain the quadrupole-octopole alignment.

V. DISCUSSION

Statistical anomalies in the large-scale CMB temperature sky measured by WMAP have been suggested as possible evidence for the violation of statistical isotropy on large scales. In any physical model for such a violation, there are testable consequences for the CMB polarization field.

We have developed a radiative-transfer simulation-based approach to predicting these consequences. We have applied this approach to modulation models of broken isotropy. In this class of models, a long-wavelength modulation of shorter-wavelength fluctuations breaks isotropy locally, while the universe remains globally isotropic and homogeneous.

A linear or dipolar modulation can be used to explain the observed power asymmetry between the northern and southern ecliptic hemispheres at multipole moments $\ell \sim 20 - 40$ [2, 5, 12, 18]. Linear modulation produces a

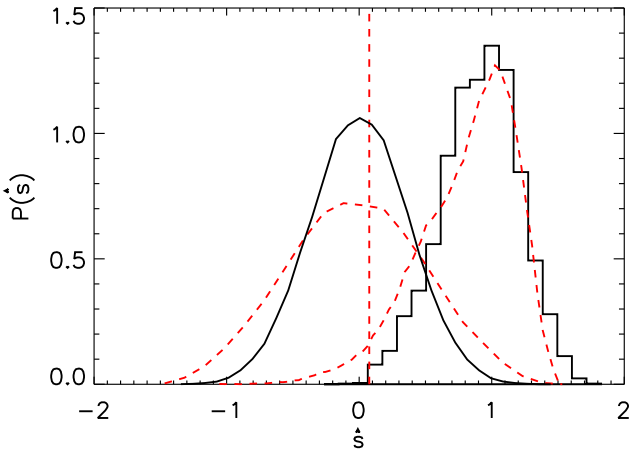

FIG. 14: Distribution of $\ell \pm 2$ correlation statistic s. Distributions on the right with $\langle \hat{s} \rangle = 1$ represent the modulated model of Eq. (24) for the joint estimator (black solid lines) and the temperature estimator (red dashed lines). Curves on the left with $\langle \hat{s} \rangle = 0$ represent the isotropic Sachs-Wolfe model in the same manner. The histogram comes from 3482 3D realizations of the modulated model and other distributions from 10^5 2D realizations. The vertical red dashed line represents the observed value for temperature only for this modulated model, using the WMAP ILC map: $\hat{s} = 0.076$.

dipole coupling that correlates multipole moments ℓ to $\ell \pm 1$ in all of the two point functions of the temperature and E polarization field. Using an analytic framework developed in the Appendix, we derive an estimator of the modulation amplitude from these fields from these correlations.

We find that the addition of polarization information substantially improves the ability to test for dipole modulation at the lowest multipoles $\ell \lesssim 10$. Under a wide range of assumptions, the dipole modulation explanation of the hemisphere asymmetry can be tested at the 98% CL or greater. These tests will require near cosmic variance limited polarization measurements at the low multipoles. Such measurements are within the statistical reach of the *Planck* satellite but systematic contamination from foregrounds will have to be sufficiently controlled.

A quadratic or quadrupolar modulation in the temperature field can be used to explain the alignment of the quadrupole and octopole [7, 17]. We generalize the considerations of Ref. [17] and develop full 3D models that enhance the probability of alignments by a factor of ~ 20.

These models predict that the quadrupole and octopole of the E-polarization will tend to align as well. However alignment of the polarization mainly tests that the temperature alignment is cosmological and originates from recombination, not the specifics of the modulation model. As such its main use will be to reject explanations of the alignments due to foregrounds or purely local secondary anisotropy. In fact a very high alignment, comparable to the temperature field, is not expected in the modulation model due to the smaller strength of the modulation at the distance to reionization. If such an alignment is seen then it is more likely that it arises from a chance configuration of the temperature field at recombination.

Quadrupolar modulation models can be distinguished in a manner similar to the dipole modulation but through a correlation between multipoles ℓ and $\ell \pm 2$ in the temperature and polarization fields. We find that the combination of temperature and polarization information out to $\ell \leq 5$ can strongly constrain the level of modulation in the low multipoles. As a consequence, polarization measurements can in principle rule out models that make the temperature alignments more than a few percent likely $\sim 99\%$ CL or stronger.

These examples illustrate that polarization in the future will provide a fruitful testing ground for explanations of the observed temperature anomalies. As predictions of anomaly models, polarization statistics move beyond the *a posteriori* inferences that currently dominate the field.

Acknowledgments

We thank Alexander Belikov, Colin Bischoff, Olivier Doré, Christopher Gordon, Gary Hinshaw, Dragan Huterer, Michael Mortonson, Kendrick Smith, and Glenn Starkman for useful discussions. We acknowledge use of the HEALPIX package and the *Legacy Archive for Microwave Background Data Analysis* (LAMBDA). This work was supported by the KICP through the grant NSF PHY-0114422. HVP was additionally supported by NASA through Hubble Fellowship grant #HF-01177.01-A awarded by the Space Telescope Science Institute, which is operated by the Association of Universities for Research in Astronomy, Inc., for NASA, under contract NAS 5-26555. WH was additionally supported by the DOE through contract DE-FG02-90ER-40560 and the David and Lucile Packard Foundation.

APPENDIX A: ANALYTIC MODULATION FRAMEWORK

In this Appendix, we construct an analytic framework for modulated temperature (§A 1) and polarization statistics (§A 2) and evaluate them explicitly for dipole modulation. We use these analytic calculations to cross check numerical results in §A 3 and to construct estimators of the dipole modulation in §A 4.

1. Modulated Temperature Field

For the temperature field, the effect of modulation can be viewed as either the direct projection of the modulated

(convolved in Fourier space) field or the convolution in harmonic space of the multipole moments of the original fields. The latter perspective is taken in Ref. [17] for the temperature field. We show in this section that the former is equivalent and more closely resembles the derivation required for polarization in §A 2.

For notational simplicity, we will derive the contribution to the spectrum due only to the modulated piece of the model of Eq. (1) so that

$$\Phi(\mathbf{x}) = g(\mathbf{x})\left[1 + h(\mathbf{x})\right] . \tag{A1}$$

The unmodulated piece can be added to these results without loss of generality.

The Fourier moments of Φ are given by a convolution of the two fields g and h,

$$\Phi(\mathbf{k}) \;=\; g(\mathbf{k}) + \int \frac{d^3k'}{(2\pi)^3} g(\mathbf{k}')h(\mathbf{k}-\mathbf{k}') , \tag{A2}$$

and the two point function of the field Φ becomes

$$\begin{aligned}\langle \Phi^*(\mathbf{k})\Phi(\mathbf{k}')\rangle =& (2\pi)^3\delta(\mathbf{k}-\mathbf{k}')P_g(k) \\ &+ \left[P_g(k) + P_g(k')\right] h(\mathbf{k}'-\mathbf{k}) \\ &+ \int \frac{d^3\tilde{k}}{(2\pi)^3} P_g(\tilde{k}) h^*(\mathbf{k}-\tilde{\mathbf{k}}) h(\mathbf{k}'-\tilde{\mathbf{k}}) .\end{aligned} \tag{A3}$$

Under the Sachs-Wolfe approximation of Eq. (5), the spherical harmonic decomposition of the temperature field yields

$$T_{\ell m} = -\frac{1}{3}\int \frac{d^3k}{(2\pi)^3} \Phi(\mathbf{k}) 4\pi i^\ell j_\ell(kD_{\rm rec}) Y^*_{\ell m}(\hat{\mathbf{k}}) , \tag{A4}$$

which implies a two-point function of the temperature harmonics of

$$\begin{aligned}\langle T^*_{\ell m} T_{\ell' m'}\rangle \;=\; & \frac{1}{9}\int \frac{d^3k}{(2\pi)^3}\int \frac{d^3k'}{(2\pi)^3} \langle \Phi^*(\mathbf{k})\Phi(\mathbf{k}')\rangle \\ & \times (4\pi)^2 i^{\ell'-\ell} j_\ell(kD_{\rm rec}) j_{\ell'}(k'D_{\rm rec}) \\ & \times Y^*_{\ell m}(\hat{\mathbf{k}}) Y_{\ell' m'}(\hat{\mathbf{k}}') .\end{aligned} \tag{A5}$$

Eqs. (A3) and (A5) provide the analytic framework for modulated temperature two-point statistics.

To make these considerations concrete, let us explicitly evaluate Eq. (A5) for dipole modulation. Dipole modulation can be taken to be a local approximation to a superhorizon scale Fourier mode,

$$\begin{aligned} h(\mathbf{x}) \;&=\; w_1 \sqrt{\frac{3}{4\pi}} \frac{1}{k_0 D_{\rm rec}} \sin\left(\mathbf{k}_0\cdot\mathbf{x}\right) \\ &\approx\; w_1 \sqrt{\frac{3}{4\pi}} \frac{z}{D_{\rm rec}} , \end{aligned} \tag{A6}$$

where we choose $\hat{\mathbf{k}}_0 \parallel \mathbf{z}$. The Fourier representation of the field becomes

$$h(\mathbf{k}) = \frac{w_1}{2i}\sqrt{\frac{3}{4\pi}} \frac{(2\pi)^3}{k_0 D_{\rm rec}} \left[\delta(\mathbf{k}-\mathbf{k}_0) - \delta(\mathbf{k}+\mathbf{k}_0)\right] . \tag{A7}$$

Now let us substitute this expression into Eq. (A3). The first term is zeroth order in h and is just the standard angular power spectrum

$$\langle T^*_{\ell m} T_{\ell' m'}\rangle^{(0)} = \delta_{\ell\ell'}\delta_{mm'} C_\ell^{TT} , \tag{A8}$$

where

$$C_\ell^{TT} = \frac{1}{9}\int \frac{dk}{k} \frac{k^3 P_g(k)}{2\pi^2} (4\pi) j_\ell^2(kD_{\rm rec}) .$$

The second term is first order in h and is given by

$$\begin{aligned}\langle T^*_{\ell m} T_{\ell' m'}\rangle^{(1)} \;=\; & \frac{1}{9}\int \frac{d^3k}{(2\pi)^3}\int d^3k' \left[P_g(k) + P_g(k')\right] \\ & \times \frac{w_1}{2i}\sqrt{\frac{3}{4\pi}} \frac{1}{k_0 D_{\rm rec}} Y^*_{\ell m}(\hat{\mathbf{k}}) Y_{\ell' m'}(\hat{\mathbf{k}}') \\ & \times \left[\delta(\mathbf{k}'-\mathbf{k}-\mathbf{k}_0) - \delta(\mathbf{k}'-\mathbf{k}+\mathbf{k}_0)\right] \\ & \times (4\pi)^2 i^{\ell'-\ell} j_\ell(kD_{\rm rec}) j_{\ell'}(k'D_{\rm rec}) .\end{aligned}$$

The simplification of these expressions requires $j_{\ell'}(k'D_{\rm rec})Y_{\ell' m'}(\hat{\mathbf{k}}')$ to be expressed in terms of $\mathbf{k}$ where $\mathbf{k}' = \mathbf{k} \pm \mathbf{k}_0$. Assuming that $k_0/k \ll 1$, we can expand,

$$\begin{aligned} & \frac{1}{k_0 D}\sqrt{\frac{3}{4\pi}} j_\ell(|\mathbf{k}+\alpha\mathbf{k}_0|D) Y_{\ell m}\left(\frac{\mathbf{k}+\alpha\mathbf{k}_0}{|\mathbf{k}+\alpha\mathbf{k}_0|}\right) \\ & \approx \frac{1}{k_0 D}\sqrt{\frac{3}{4\pi}} j_\ell(kD) Y_{\ell m}(\hat{\mathbf{k}}) \\ & \quad - \alpha R^{1,\ell+1}_{\ell m} j_{\ell+1}(kD) Y_{\ell+1,m}(\hat{\mathbf{k}}) \\ & \quad + \alpha R^{1,\ell-1}_{\ell m} j_{\ell-1}(kD) Y_{\ell-1,m}(\hat{\mathbf{k}}) , \end{aligned} \tag{A9}$$

where the coupling matrix $R^{\ell_1,\ell_2}_{\ell m}$ is defined as [29]

$$\begin{aligned} R^{\ell_1,\ell_2}_{\ell m} =& (-1)^m \sqrt{\frac{(2\ell+1)(2\ell_1+1)(2\ell_2+1)}{4\pi}} \\ & \times \begin{pmatrix} \ell_1 & \ell_2 & \ell \\ 0 & 0 & 0 \end{pmatrix} \begin{pmatrix} \ell_1 & \ell_2 & \ell \\ 0 & m & -m \end{pmatrix} . \end{aligned} \tag{A10}$$

With these relations, the first order term in h becomes

$$\langle T^*_{\ell m} T_{\ell' m'}\rangle^{(1)} = \delta_{mm'} w_1 \left[R^{1,\ell}_{\ell' m} C_\ell^{TT} + R^{1,\ell'}_{\ell m} C_{\ell'}^{TT}\right] . \tag{A11}$$

By virtue of the Wigner $3j$ symbol in the coupling matrix, the dipole modulation couples ℓ to $\ell \pm 1$ with a strength that is linear in h or w_1.

Likewise, the same operations on the term quadratic in h yield

$$\langle T^*_{\ell m} T_{\ell' m'}\rangle^{(2)} = \delta_{mm'} w_1^2 \left[\sum_{\ell_1} R^{1,\ell_1}_{\ell m} R^{1,\ell_1}_{\ell' m} C_{\ell_1}^{TT}\right] . \tag{A12}$$

The quadratic term in h or w_1 couples ℓ to $\ell \pm 2$. These results are the same as obtained in Ref. [17].

2. Modulated Polarization Field

For predicting polarization statistics, the direct angular modulation approach of [17] does not apply given that the sources of the polarization field are modulated and not the field itself.

The quadrupole source comes from the temperature field through Eq. (9)

$$T_{2m}(\mathbf{x}) = -\int d\hat{\mathbf{n}}' Y^*_{2m}(\hat{\mathbf{n}}')\frac{\Phi(\mathbf{x}')}{3}\,, \tag{A13}$$

where recall $\mathbf{x}' = \mathbf{x} + \Delta D\hat{\mathbf{n}}'$ (see Fig. 2).

Decomposing Φ into Fourier modes yields

$$T_{2m}(\mathbf{x}) = \int \frac{d^3k}{(2\pi)^3}\frac{\Phi(\mathbf{k})}{3}4\pi j_2(k\Delta D)Y^*_{2m}(\hat{\mathbf{k}})e^{i\mathbf{k}\cdot\mathbf{x}}. \tag{A14}$$

The Stokes parameters of the polarization are given by Eq. (12)

$$\begin{aligned}
&(Q \pm iU)(\hat{\mathbf{n}}) \qquad\qquad (A15)\\
&= -\frac{\sqrt{6}}{10}\int dD\frac{d\tau}{dD}e^{-\tau}\sum_m T_{2m}(D\hat{\mathbf{n}})_{\pm2}Y_{2m}(\hat{\mathbf{n}})\\
&= -\frac{\sqrt{6}}{10}\int dD\frac{d\tau}{dD}e^{-\tau}\frac{1}{3}\int\frac{d^3k}{(2\pi)^3}\Phi(\mathbf{k})(4\pi)^2\\
&\quad\times j_2(k\Delta D)\sum_{\ell'} i^{\ell'}j_{\ell'}(kD)\\
&\quad\times\sum_{m_2m'} Y^*_{2m_2}(\hat{\mathbf{k}})Y^*_{\ell'm'}(\hat{\mathbf{k}})Y_{\ell'm'}(\hat{\mathbf{n}})_{\pm2}Y_{2m_2}(\hat{\mathbf{n}})\,.
\end{aligned}$$

Recoupling the last line of Eq. (A15), we have

$$\begin{aligned}
&\sum_{m_2m'} Y^*_{2m_2}(\hat{\mathbf{k}})Y^*_{\ell'm'}(\hat{\mathbf{k}})Y_{\ell'm'}(\hat{\mathbf{n}})_{\pm2}Y_{2m_2}(\hat{\mathbf{n}}) =\\
&\quad\sum_{\ell m}\frac{(2\ell'+1)5}{4\pi}\begin{pmatrix}\ell' & 2 & \ell\\ 0 & \mp2 & \pm2\end{pmatrix}\begin{pmatrix}\ell' & 2 & \ell\\ 0 & 0 & 0\end{pmatrix}\\
&\quad\times{}_{\pm2}Y_{\ell m}(\hat{\mathbf{n}})Y^*_{\ell m}(\hat{\mathbf{k}})\,. \qquad (A16)
\end{aligned}$$

Decomposing into the spin-2 spherical harmonics,

$$\begin{aligned}
&E_{\ell m} \pm iB_{\ell m} = -\int d\hat{\mathbf{n}}\,{}_{\pm2}Y^*_{\ell m}(\hat{\mathbf{n}})(Q\pm iU)(\hat{\mathbf{n}})\\
&= \frac{\sqrt{6}}{10}\int dD\frac{d\tau}{dD}e^{-\tau}\frac{1}{3}\int\frac{d^3k}{(2\pi)^3}\Phi(\mathbf{k})\\
&\quad\times(4\pi)^2 j_2(k\Delta D)\sum_{\ell'} i^{\ell'}j_{\ell'}(kD) \qquad (A17)\\
&\quad\times\frac{(2\ell'+1)5}{4\pi}\begin{pmatrix}\ell' & 2 & \ell\\ 0 & \mp2 & \pm2\end{pmatrix}\begin{pmatrix}\ell' & 2 & \ell\\ 0 & 0 & 0\end{pmatrix}Y^*_{\ell m}(\hat{\mathbf{k}})\,.
\end{aligned}$$

Note that the B-modes vanish since the second Wigner $3j$ symbol is zero if $(\ell+\ell'+2)$ is odd and

$$\begin{pmatrix}\ell' & 2 & \ell\\ 0 & 2 & -2\end{pmatrix} = (-1)^{\ell+\ell'}\begin{pmatrix}\ell' & 2 & \ell\\ 0 & -2 & 2\end{pmatrix}\,. \tag{A18}$$

This is to be expected since all scalar sources, even products of fundamental scalars, generate only E-modes.

Paralleling the modulated temperature derivation of §A 1, we find that there is the zeroth order piece coming from the unmodulated field that reproduces the standard result [28].

$$\langle E^*_{\ell m}E_{\ell'm'}\rangle^{(0)} = \delta_{\ell\ell'}\delta_{mm'}C^{EE}_\ell\,, \tag{A19}$$

where

$$C^{EE}_\ell = \frac{1}{6}\int\frac{dk}{k}\frac{k^3P_g}{2\pi^2}4\pi I^2_\ell(k)\,, \tag{A20}$$

with

$$I_\ell(k) = \int dD\frac{d\tau}{dD}e^{-\tau}j_2(k\Delta D)\epsilon^{(0)}_\ell(kD)\,, \tag{A21}$$

and the polarization radial function

$$\epsilon^{(0)}_\ell(x) = \sqrt{\frac{3}{8}\frac{(\ell+2)!}{(\ell-2)!}}\frac{j_\ell(x)}{x^2}\,. \tag{A22}$$

The linear piece in h of the dipole modulation becomes

$$\begin{aligned}
\langle E^*_{\ell m}E_{\ell'm'}\rangle^{(1)} &= \frac{(4\pi)^2}{6}\frac{w_1}{2}\sqrt{\frac{3}{4\pi}}\frac{1}{k_0D_{\rm rec}}\\
&\times\int\frac{d^3k}{(2\pi)^3}\int\frac{d^3k'}{(2\pi)^3}\left[P_g(k)+P_g(k')\right]\\
&\times(2\pi)^3\left[\delta(\mathbf{k}'-\mathbf{k}-\mathbf{k}_0)-\delta(\mathbf{k}'-\mathbf{k}+\mathbf{k}_0)\right]\\
&\times\left[\int dD\frac{d\tau}{dD}e^{-\tau}j_2(k\Delta D)\epsilon^{(0)}_\ell(kD)\right]\\
&\times\left[\int dD\frac{d\tau}{dD}e^{-\tau}j_2(k'\Delta D)\epsilon^{(0)}_{\ell'}(k'D)\right]\\
&\times i^{\ell'-\ell-1}Y_{\ell m}(\hat{\mathbf{k}})Y^*_{\ell'm'}(\hat{\mathbf{k}}')\,. \qquad (A23)
\end{aligned}$$

Assuming, as in the temperature case, that $k/k_0 \ll 1$, we can again Taylor expand the spherical Bessel functions and the spherical harmonic which, after some algebra, reduces Eq. (A23) to

$$\begin{aligned}
\langle E^*_{\ell m}E_{\ell'm'}\rangle^{(1)} = \delta_{mm'}w_1R^{1,\ell}_{\ell'm}\Big[&\sqrt{\frac{(\ell'+2)!(\ell-2)!}{(\ell'-2)!(\ell+2)!}}A_\ell\\
&+(\delta_{\ell,\ell'+1}-\delta_{\ell,\ell'-1})B_{\ell\ell'}\Big]+(\ell\leftrightarrow\ell')\,,
\end{aligned} \tag{A24}$$

where

$$\begin{aligned}
A_\ell &= \frac{1}{6}\int\frac{dk}{k}\frac{k^3P_g}{2\pi^2}4\pi I_\ell(k)J_\ell(k)\,,\\
B_{\ell\ell'} &= \frac{1}{6}\int\frac{dk}{k}\frac{k^3P_g}{2\pi^2}4\pi I_\ell(k)K_{\ell'}(k)\,,
\end{aligned} \tag{A25}$$

and

$$\begin{aligned}
J_\ell(k) &= \int dD\frac{d\tau}{dD}e^{-\tau}\frac{D}{D_{\rm rec}}j_2(k\Delta D)\epsilon^{(0)}_\ell(kD)\,,\\
K_\ell(k) &= \int dD\frac{d\tau}{dD}e^{-\tau}\frac{\Delta D}{D_{\rm rec}}j_3(k\Delta D)\epsilon^{(0)}_\ell(kD)\,,
\end{aligned} \tag{A26}$$

with $I_\ell(k)$ defined in Eq. (A21). Like the temperature field, the coupling of ℓ to $\ell\pm1$ is linear in h. The quadratic term can be similarly calculated but is more cumbersome and we omit the derivation here.

For reasonable reionization histories, the dominant term in Eq. (A24) is the first term. Comparing Eq. (A20) with (A26) we see that to order of magnitude,

$$A_\ell \sim \frac{\bar{D}}{D_{\rm rec}} C_\ell^{EE}\,, \tag{A27}$$

where $\bar{D}$ is a typical distance to reionization. Compared with the modulation of the temperature spectrum in Eq. (A11), the modulation of the polarization spectrum is suppressed by a factor of $\bar{D}/D_{\rm rec}$. This factor is due to the lower level of spatial modulation at typical distances to reionization in the dipolar model of Eq. (A6). Typically, it has a value of $\bar{D}/D_{\rm rec} \sim 2/3$.

For the TE two point function, the same operations yield

$$\begin{aligned}\langle T^*_{\ell m} E_{\ell' m'}\rangle^{(1)} =& \delta_{mm'} w_1 R^{1,\ell}_{\ell' m}\Big[\sqrt{\frac{(\ell'+2)!(\ell-2)!}{(\ell'-2)!(\ell+2)!}} H_\ell + \\ &+ (\delta_{\ell,\ell'+1} - \delta_{\ell,\ell'-1}) L_{\ell\ell'}] + C^{TE}_{\ell'}\Big]\,,\end{aligned} \tag{A28}$$

with

$$\begin{aligned} H_\ell =& \frac{1}{\sqrt{54}} \int \frac{dk}{k} \frac{k^3 P_g}{2\pi^2} j_\ell(kD_{\rm rec}) 4\pi J_\ell(k)\,, \\ L_{\ell\ell'} =& \frac{1}{\sqrt{54}} \int \frac{dk}{k} \frac{k^3 P_g}{2\pi^2} j_\ell(kD_{\rm rec}) 4\pi K_{\ell'}(k)\,, \end{aligned} \tag{A29}$$

where C_ℓ^{TE} is the usual unmodulated cross power spectrum

$$C_\ell^{TE} = \frac{1}{\sqrt{54}} \int \frac{dk}{k} \frac{k^3 P_g(k)}{2\pi^2} 4\pi j_\ell(kD_{\rm rec}) I_\ell(k)\,, \tag{A30}$$

and $I_\ell(k)$ is defined in Eq. (A21).

3. Comparison with Simulations

In this section, we test the 3D simulation method against the analytic results of §A 1 and A 2. The simulations are performed according to the algorithm described in Section II D with a box of size that is four times the diameter of the last scattering surface and a spatial resolution defined by the 512^3 pixels.

We first test the simulations against the usual results given by Eq. (A9), (A20), and (A30) for an unmodulated scale invariant potential spectrum. The temperature power spectra averaged over multiple realizations agrees with the analytic results within the sample variance

$$\frac{\Delta C_\ell^{TT}}{C_\ell^{TT}} = \sqrt{\frac{2}{(2\ell+1)N}}\,, \tag{A31}$$

where N is the number of simulated skies.

In order to predict the E-modes, we calculate the quadrupolar temperature sources for 80 radii along each line of sight, and in every unit vector $\hat{\mathbf{n}}$ corresponding to 12,288 HEALPIX pixel centers at resolution $N_{\rm side} = 32$. The small evolution of perturbations of the potential field between recombination and reionization is accounted for via the transfer function.

We compute the E modes for different reionization histories with ionization fraction equal to 1 out to a redshift where the optical depth $\tau = \{0.0279, 0.055, 0.089\}$ and zero beyond this redshift. In all cases, the distribution of numerical spectra are consistent with cosmic variance for $\ell \leq 10$. For larger multipoles there is a diminution of power that is consistent with the Nyquist frequency of the box, but this does not affect any of our results.

Finally, we check the dipole modulation model against the analytic results of the previous sections. We showed there that a dipole modulation gives rise to couplings between ℓ and $\ell' = \ell \pm 1$ modes in the TT, EE, TE and ET two point functions. As an example of these correlations, we compare simulation results with the analytic calculation in Fig. 15. We again find agreement within sample variance expectations.

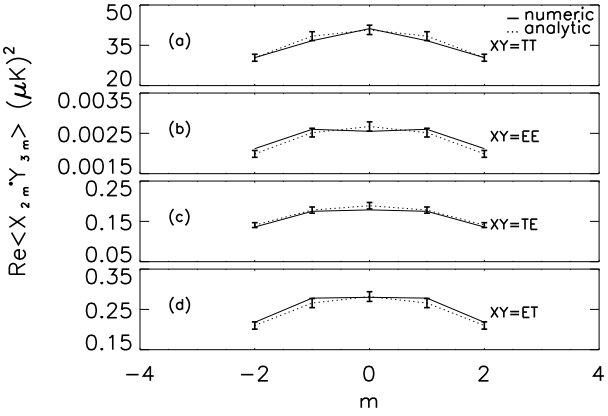

FIG. 15: Comparison between analytical solution (dotted line) and 545 3D simulations (solid line) of the dipole modulation model with $w_1 = 0.2$. The two point correlation between the quadrupole and octopole m moments are shown for the X and Y fields: $XY = TT$, EE, TE, ET. Error bars reflect the sample variance expected for 545 skies.

4. Dipolar Modulation Estimators

From the analytic calculations of §A 1 and A 2, we can construct unbiased estimators of the dipole modulation amplitude w_1. In the presence of a dipole modulation, the expectation values of temperature and polarization modes ℓ and $\ell' = \ell \pm 1$ are correlated. Each pair of

multipoles then forms an estimator of w_1

$$\hat{w}^{XY}_{1,\ell m} = \frac{X^*_{\ell m} Y_{\ell+1,m}}{f^{XY}_\ell R^{1\ell}_{\ell+1,m}}\,, \tag{A32}$$

where $XY \in \{TT, EE, ET, TE\}$, $R^{1\ell}_{\ell+1,m}$ are coupling matrices defined in Eq. (A10) and the coefficients f^{XY}_ℓ are given by

$$\langle X^*_{\ell m} Y_{\ell+1,m}\rangle = f^{XY}_\ell R^{1\ell}_{\ell+1,m} w_1\,, \tag{A33}$$

such that $\langle \hat{w}^{XY}_{1,\ell m}\rangle = w_1$. Specifically, Eqs. (A11), (A24), and (A28) give

$$\begin{aligned}
f^{TT}_\ell =& C^{TT}_\ell + C^{TT}_{\ell+1}\,, \qquad (A34)\\
f^{EE}_\ell =& \sqrt{\frac{(\ell+3)!(\ell-2)!}{(\ell-1)!(\ell+2)!}} A_\ell - B_{\ell,\ell+1} + (\ell \leftrightarrow \ell+1)\,,\\
f^{TE}_\ell =& \sqrt{\frac{(\ell+3)!(\ell-2)!}{(\ell-1)!(\ell+2)!}} H_\ell - L_{\ell,\ell+1} + C^{TE}_{\ell+1}\,,\\
f^{ET}_\ell =& \sqrt{\frac{(\ell+2)!(\ell-1)!}{(\ell-2)!(\ell+3)!}} H_{\ell+1} + L_{\ell+1,\ell} + C^{TE}_\ell\,,
\end{aligned}$$

where A_ℓ, $B_{\ell,\ell+1}$, H_ℓ and $L_{\ell,\ell+1}$ are given by Eqs. (A25) and (A29).

Each estimator carries a large sample variance and so one can combine them to form the joint estimator

$$\hat{w}_1 = \sum_{XY}\sum_{\ell,m} A^{XY}_{\ell m}\, \hat{w}^{XY}_{1,\ell m}\,, \tag{A35}$$

where $A^{XY}_{\ell m}$ are the weights assigned to each one. To maintain the condition that the estimator is unbiased $\langle \hat{w}_1\rangle = w_1$, the weights must satisfy

$$\sum_{XY}\sum_{\ell m} A^{XY}_{\ell m} = 1\,. \tag{A36}$$

Note that while individual $\hat{w}^{XY}_{1,\ell m}$ estimators are complex, the joint estimator is real if $+m$ and $-m$ are combined with equal weights.

We employ weights that minimize the variance of the joint estimator. Given a model with $w_1 = 0$, the variance is

$$\langle \hat{w}^2_1\rangle = \sum_{XY,X'Y'}\sum_{\ell m} A^{XY}_{\ell m} A^{X'Y'}_{\ell m} \frac{\mathcal{C}^{(\ell)}_{XY,X'Y'}}{(R^{1\ell}_{\ell+1,m})^2}\,. \tag{A37}$$

Here $\mathcal{C}^{(\ell)}_{XY,X'Y'}$ are the components of the matrix $\mathcal{C}$ given by

$$\mathcal{C}^{(\ell)}_{XY,X'Y'} = \frac{C^{XX'}_\ell C^{YY'}_{\ell+1}}{f^{XY}_\ell f^{X'Y'}_\ell}\,, \tag{A38}$$

where $C^{XX'}_\ell$ are the standard angular power spectra coefficients.

Imposing the normalization constraint on the weights, given by Eq. (A36), we minimize the variance with

$$A^{XY}_{\ell m} = \frac{\sum_{X'Y'} [\mathcal{C}^{(\ell)}]^{-1}_{XY,X'Y'} (R^{1\ell}_{\ell+1,m})^2}{\sum_{XY,X'Y'}\sum_{\ell m} [\mathcal{C}^{(\ell)}]^{-1}_{XY,X'Y'} (R^{1\ell}_{\ell+1,m})^2}\,, \tag{A39}$$

which is the usual inverse covariance weight of covarying estimators. Likewise in the case that just one of the XY combinations is used this general form reduces to

$$\hat{w}^{XY}_1 = \frac{\sum_{\ell m} \frac{f^{XY}_\ell R^{1\ell}_{\ell+1,m}}{C^{XX}_\ell C^{YY}_{\ell+1}} X^*_{\ell m} Y_{\ell+1,m}}{\sum_{\ell m} \frac{(f^{XY}_\ell R^{1\ell}_{\ell+1,m})^2}{C^{XX}_\ell C^{YY}_{\ell+1}}}\,, \tag{A40}$$

which is the usual inverse variance weighted estimator. Note that the sum over ℓ can be restricted to $\ell \le \ell_{\rm max}$ for modulation models which only affect large scales.

Finally, given instrumental noise power spectra N^{XY}_ℓ, the variance and minimum variance weights are modified by including the spectrum into the covariance matrix

$$\mathcal{C}^{(\ell)}_{XY,X'Y'} = \frac{(C^{XX'}_\ell + N^{XX'}_\ell)(C^{YY'}_{\ell+1} + N^{YY'}_{\ell+1})}{f^{XY}_\ell f^{X'Y'}_\ell}\,, \tag{A41}$$

where we typically assume that the noise cross power spectrum TE vanishes.

[1] C. L. Bennett et al. (WMAP), Astrophys. J. Suppl. **148**, 1 (2003), astro-ph/0302207.
[2] D. N. Spergel et al. (WMAP), Astrophys. J. Suppl. **148**, 175 (2003), astro-ph/0302209.
[3] G. Hinshaw et al. (WMAP) (2006), astro-ph/0603451.
[4] L. Page et al. (WMAP) (2006), astro-ph/0603450.
[5] H. K. Eriksen, F. K. Hansen, A. J. Banday, K. M. Gorski, and P. B. Lilje, Astrophys. J. **605**, 14 (2004), astro-ph/0307507.
[6] K. Land and J. Magueijo, Mon. Not. Roy. Astron. Soc. **362**, 838 (2005), astro-ph/0502574.
[7] A. de Oliveira-Costa, M. Tegmark, M. Zaldarriaga, and A. Hamilton, Phys. Rev. **D69**, 063516 (2004), astro-ph/0307282.
[8] C. J. Copi, D. Huterer, and G. D. Starkman, Phys. Rev. **D70**, 043515 (2004), astro-ph/0310511.
[9] M. Tegmark, A. de Oliveira-Costa, and A. J. S. Hamilton, Phys. Rev. D **68**, 123523 (2003).
[10] D. J. Schwarz, G. D. Starkman, D. Huterer, and C. J. Copi, Phys. Rev. Lett. **93**, 221301 (2004), astro-ph/0403353.
[11] K. Land and J. Magueijo, Phys. Rev. Lett. **95**, 071301 (2005), astro-ph/0502237.
[12] H. K. Eriksen, A. J. Banday, K. M. Gorski, F. K. Hansen, and P. B. Lilje, Astrophys. J. **660**, L81 (2007), astro-ph/0701089.

[13] C. J. Copi, D. Huterer, D. J. Schwarz, and G. D. Starkman, Mon. Not. Roy. Astron. Soc. **367**, 79 (2006), astro-ph/0508047.
[14] C. Copi, D. Huterer, D. Schwarz, and G. Starkman, Phys. Rev. **D75**, 023507 (2007), astro-ph/0605135.
[15] Y. Wiaux, P. Vielva, E. Martinez-Gonzalez, and P. Vandergheynst, Phys. Rev. Lett. **96**, 151303 (2006), astro-ph/0603367.
[16] K. Land and J. Magueijo, Mon. Not. Roy. Astron. Soc. **357**, 994 (2005), astro-ph/0405519.
[17] C. Gordon, W. Hu, D. Huterer, and T. Crawford, Phys. Rev. **D72**, 103002 (2005), astro-ph/0509301.
[18] C. Gordon, Astrophys. J. **656**, 636 (2007), astro-ph/0607423.
[19] R. Sachs and A. Wolfe, Astrophys. J. Suppl. **147**, 73 (1967).
[20] W. Hu, Astrophys. J. **529**, 12 (2000), astro-ph/9907103.
[21] K. M. Gorski, B. D. Wandelt, F. K. Hansen, E. Hivon, and A. J. Banday (1999), astro-ph/9905275.
[22] R. R. Caldwell, R. Dave, and P. J. Steinhardt, Phys. Rev. Lett. **80**, 1582 (1998), astro-ph/9708069.
[23] W. Hu, Astrophys. J. **506**, 485 (1998), astro-ph/9801234.
[24] R. Bean and O. Dore, Phys. Rev. **D69**, 083503 (2004), astro-ph/0307100.
[25] C. Gordon and W. Hu, Phys. Rev. D **70**, 083003 (2004), astro-ph/0406496.
[26] K. T. Inoue and J. Silk, Astrophys. J. **648**, 23 (2006), astro-ph/0602478.
[27] C. Vale (2005), astro-ph/0509039.
[28] W. Hu and M. J. White, Phys. Rev. **D56**, 596 (1997), astro-ph/9702170.
[29] The normalization differs from Ref. [17] by w_ℓ.